Nano-Micro Letters

e-ISSN 2150-5551
CN 31-2103/TB

ARTICLE

https://doi.org/10.1007/s40820-023-01275-3

Cite as
Nano-Micro Lett.
(2024) 16:55

Received: 10 August 2023
Accepted: 8 November 2023


# Enhanced Redox Electrocatalysis in High-Entropy Perovskite Fluorides by Tailoring *d–p* Hybridization

Xudong Li[1], Zhuomin Qiang[2] ✉, Guokang Han[2] ✉, Shuyun Guan[1], Yang Zhao[1], Shuaifeng Lou[2], Yongming Zhu[1] ✉

## HIGHLIGHTS

- The tailored KCoMnNiMgZnF$_3$-HEC cathode delivers extremely high discharge capacity (22,104 mAh g$^{-1}$), outstanding long-term cyclability (over 500 h), preceding majority of traditional catalysts reported.
- Entropy effect of multiple sites in KCoMnNiMgZnF$_3$-HEC engenders appropriate regulation of 3*d* orbital structure, leading to a moderate hybridization with the *p* orbital of key intermediate.
- The homogeneous nucleation of $Li_2O_2$ is achieved on multiple cation site, contributing to effective mass transfer at the three-phase interface, and thus, the reversibility of $O_2/Li_2O_2$ conversion.

**ABSTRACT** High-entropy catalysts featuring exceptional properties are, in no doubt, playing an increasingly significant role in aprotic lithium-oxygen batteries. Despite extensive effort devoted to tracing the origin of their unparalleled performance, the relationships between multiple active sites and reaction intermediates are still obscure. Here, enlightened by theoretical screening, we tailor a high-entropy perovskite fluoride (KCoMnNiMgZnF$_3$-HEC) with various active sites to overcome the limitations of conventional catalysts in redox process. The entropy effect modulates the *d*-band center and d orbital occupancy of active centers, which optimizes the *d–p* hybridization between catalytic sites and key intermediates, enabling a moderate adsorption of $LiO_2$ and thus reinforcing the reaction kinetics. As a result, the Li–$O_2$ battery with KCoMnNiMgZnF$_3$-HEC catalyst delivers a minimal discharge/charge polarization and long-term cycle stability, preceding majority of traditional catalysts reported. These encouraging results provide inspiring insights into the electron manipulation and *d* orbital structure optimization for advanced electrocatalyst.

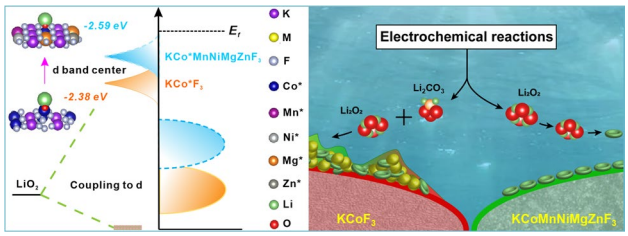


**KEYWORDS** Lithium–oxygen batteries; KCoMnNiMgZnF$_3$-HEC perovskite fluoride; Entropy effect; Catalytic kinetics; *d–p* orbital hybridization

✉ Zhuomin Qiang, 21b925049@stu.hit.edu.cn; Guokang Han, gkhan@hit.edu.cn; Yongming Zhu, hitonline@163.com
[1] Department of Applied Chemistry, Harbin Institute of Technology at Weihai, Weihai 264209, People's Republic of China
[2] MIIT Key Laboratory of Critical Materials Technology for New Energy Conversion and Storage, School of Chemistry and Chemical Engineering, Harbin Institute of Technology, Harbin 150001, People's Republic of China

Published online: 18 December 2023

Shanghai Jiao Tong University Press

Springer

## 1 Introduction

Rechargeable lithium–oxygen battery (LOB) has drawn intriguing attraction owing to its ultrahigh theoretical energy density (3500 Wh $kg^{-1}$), which can be expected to become ultimate candidate to replace current state-of-the-art lithium-ion battery [1]. Nevertheless, LOB suffers from low round-trip efficiency and poor cyclability, accompanied with large polarization. Those intractable issues mainly lie in the sluggish oxygen reduction reaction (ORR) and oxygen evolution reaction (OER), closely related to the complex $O_2/Li_2O_2$ redox chemistry in the air cathodes [2]. The reversibility of $Li_2O_2$ deposition/decomposition directly determines the performance of LOB, highlighting the necessity of ameliorating reaction kinetics through constructing well-tailored catalysts. It is widely accepted that catalyst activity depends substantially on the adsorption/desorption of intermediates on surface-active sites, which can be modulated via tuning orbital occupancy of active centers [3–5]. Various elaborate catalysts with *d*-block transition metals, as $LiO_2$-affinity regulators, have been rapidly explored in recent years to boosting catalytic conversion of $O_2/Li_2O_2$ in LOBs [6–10]. Despite the considerable optimization in catalytic kinetics, the functionality and availability of such catalysts still fall short of expectations, mainly due to the limited number of accessible active sites.

High entropy compounds (HECs), a new frontier in catalysis with broad chemical space tunability, have shown particularly high catalytic activities compared to conventional mono- and bimetallic nanocrystals [11, 12]. Infinite elemental combinations enrich the diversities of active sites and local electronic structures, which provides more possibilities for tailoring of functional properties, and thus expands a wide design platform for catalysts with desirable activity, durability, and effectivity. Theoretically, synergistic effect and interaction of dissimilar species can enhance site-to-site electron transfer, allowing simultaneous stabilization of reaction intermediates with moderate binding energies in multi-steps/electron/phase redox conversions of LOB electrochemistry. A majority of works have been dedicated to the exploration of catalytic performance for HECs, and however, the understanding of activity origins and correlations between intrinsic electronic structure and reaction intermediates in HECs is greatly neglected [13–15]. Furthermore, the influence of multiple active sites on the nucleation/growth kinetics of $Li_2O_2$ in redox processes remains ambiguous, hindering the selection and rational design of HECs catalysts for LOBs.

Herein, a sophisticated $KCoMnNiMgZnF_3$, and HEC-perovskite fluoride, was first introduced into LOBs to overcome the limitations of conventional catalysts in redox process. We systematically investigated the local electronic environments of cation sites and identified *d*-band-dependent preferences for the adsorption of reaction intermediates during catalysis. The density function theory (DFT) calculations revealed that the *d*-band center and *d* orbital occupancy of active centers can be regulated by entropy effect, which engenders a favorable *d-p* orbital hybridization between multiple active cations in HEC and $LiO_2$. This moderate interaction grants $KCoMnNiMgZnF_3$-HEC the enhanced catalytic kinetics, effectively lowering the redox energy barrier. Experimental analysis combined with COMSOL multiphysics demonstrated that the multiple active sites in $KCoMnNiMgZnF_3$-HEC moiety served as nucleation seeds synergistically facilitate the homogeneous formation of $Li_2O_2$, which in favor of the mass transfer, leading to an impressive electrochemical performance of LOB. The LOB with $KCoMnNiMgZnF_3$-HEC catalyst achieves a very low overall discharge/charge overpotential (0.7 V), extremely high discharge capacity (22,104 mAh $g^{-1}$ at a current density of 200 mA $g^{-1}$) and outstanding long-term cyclability (over 500 cycles at a current density of 1000 mA $g^{-1}$ with a capacity limitation of 1000 mAh $g^{-1}$), which is superior to that of the current traditional catalysts. Our work suggests the possibility of manipulating the reaction kinetics and nucleation/growth mechanisms of $Li_2O_2$ by the unique entropy effect of multiple sites in HEC, providing guidance to the rational design of efficient active sites for LOBs.

## 2 Experimental Section

### 2.1 Materials

Cobalt chloride hexahydrate ($CoCl_2{\cdot}6H_2O$, AR), nickel(II) chloride hexahydrate ($NiCl_2{\cdot}6H_2O$, AR), manganese chloride tetrahydrate ($MnCl_2{\cdot}4H_2O$, AR), zinc chloride ($ZnCl_2$, AR), Potassium fluoride dihydrate


https://doi.org/10.1007/s40820-023-01275-3

($KF{\cdot}2H_2O$, AR), polyvinyl pyrrolidone (PVP-K29-32, AR) and ethylene glycol ($C_2H_6O_2$, AR) were supplied from Shanghai Aladdin Biochemical Technology Co., Ltd. (China). The CR2032 cell, glass fiber separator (GF/B), lithium bis(trifluoromethanesulphonyl)imide ($LiN(CF_3SO_2)_2$), ≥ 99.9 wt%), tetraethylene glycol dimethyl ether ($C_{10}H_{22}O_5$, ≥ 99.5%(GC)), Ketjen Black (KB EC-600JD), lithium foil and carbon paper (H060) were purchased by Aisim (Shenzhen) Technology Co., Ltd. (China).

## 2.2 Preparation of GO, HCPA and GO/HCPA Nanocomposite Papers

### 2.2.1 Preparations of the $KCoF_3$, $KCoMnNiF_3$, $KCoMnNiMgF_3$ and $KCoMnNiZnF_3$ Samples

Perovskite fluorides were synthesized accordant with reference as reported, but with some modifications here. Taking the $KCoMnNiZnF_3$-HEC as a representative, 0.8 mmol $CoCl_2{\cdot}6H_2O$, 0.8 mmol $NiCl_2{\cdot}6H_2O$, 0.8 mmol $MnCl_2{\cdot}4H_2O$, 0.8 mmol $MgCl_2$, 0.8 mmol $ZnCl_2$, 10 mmol $KF{\cdot}2H_2O$ and 0.4 g PVP-K29-32 were added into in 72 mL ethylene glycol solvent. After dissolving completely, the mixture was treated solvent thermally in a teflon-lined stainless-steel autoclave at 180 °C for 12 h in a homogeneous reactor, and allowed to cool-down naturally. Subsequently, the sample was washed with absolute alcohol, repeated several times until the solution clean up. Finally, the compound was dried in vacuum at 80 °C, obtaining the $KCoMnNiZnF_3$-HEC material. As for other samples, the synthetic process complied with the above procedure, according to their metallic element ratios with the total molar ratio of 4 mmol.

### 2.2.2 Materials Characterizations

The X-ray diffraction (XRD) was performed on a Rigaku D/max-rb diffractometer equipped with Cu Kα radiation ($\lambda = 1.5406$ Å, 40 kV, 20 mA). Transmission electron microscopy (TEM) and high-angle annular dark-field scanning transmission electron microscopy (HAADF-STEM) images were recorded on JEOL JEM2100 microscope operated at 200 kV. Energy dispersive spectroscopy (EDS) was conducted on NORAN system 7 equipped with TEM. PerkinElmer Optima 5300DV ICP-OES system was used to determine the mass fraction of elements. The X-ray photoelectron spectroscopy (XPS) was carried out on Physical Electronics PHI model 5700 instrument with Al Kα radiation. The XAFS spectra were measured on Super Photon ring-8 of the Japan Synchrotron Radiation Research Institute. The electron paramagnetic resonance (EPR) spectroscopy was determined with JEOL JES-X-320 operating at X-band frequency of 9.79 GHz. The Co K-edge XANES data were accounted in transmission mode with Co foil, CoO and $Co_3O_4$ as references. The obtained EXAFS data was processed based on the standard routine utilizing the Athena software packages. The EXAFS spectra were obtained by deducing the post-edge background from the overall absorption and then normalizing in respect of the edge-jump step. Raman spectroscopy (Raman) was were collected on Invia-Reflex of Renishaw with wavelength of 532 nm. The scanning electron microscopy (SEM) was conducted on Helios Nanolab 600i at 20 kV. The in-situ differential electrochemical mass spectrometry was tested at HPR20-EGA.

### 2.2.3 Electrochemical Measurements

*Li–$O_2$ cell assembly and testing* the perovskite fluorides catalysts (30%) and Ketjen Black EC-600JD (KB, 50%) were uniform mixed with polyvinyl pyrrolidone (PVP, 20%) binder in mixture (isopropanol/water = 1:3) to form a homogeneous ink, which was sprayed on a piece of carbon paper ($D = 14$ mm). After vacuum drying at 80 °C for 12 h, the $O_2$-electrodes were obtained. The electrolyte adopted 1 M lithium bis(trifluoromethane)sulfonimide (LiTFSI) in triethylene glycol dimethyl ether (TEGDME). The anode and separator used lithium foils and Whatman GF/D glass fibers, respectively. The 2032-tyoe coin cells were assembled in an argon-filled glovebox with oxygen and moisture contents below 0.1 ppm. The galvanostatic charge–discharge performances were conducted on a battery test system (LAND, China) at different current densities in the voltage scope of 2.0–4.5 V versus Li/$Li^+$, or in a capacity limitation. The cyclic stability measures were conducted under a limited capacity. All the evaluation tests mentioned above were carried out at room temperature.

### 2.2.4 Computational Calculations and Simulations

*The density functional theory (DFT) calculations* the DFT were conducted on the Vienna ab initio simulation package (VASP). The models were constructed based on $KCoF_3$

(110) (17.7 Å × 8.35 Å × 11.25 Å), and the vacuum depth was set to 20 Å. The 3*d*/4*s* electrons of Co, Ni, Mn and Zn atoms, 2*s*/2*p* electrons for F, 2*s*/2*p*/3*s* electrons for Mg, and 4*s*/3*p*/4*s* electrons for K were treated as valence electrons. The generalized gradient approximation (GGA) were used as the gradient correction function (Perdew–Burke–Ernzerhof (PBE). The interaction between valence electrons and core electrons was described by the plane-mode conserved pseudopotential (PAW). The dispersion interactions were described by Grimme's DFT-D3 methodology. The 2 × 3 × 1 grid points were performed using the Monkhorst–Pack method in the Brillouin region with plane wave truncation energy of 400 eV. In the optimization process, the energy convergence accuracy was set to $1.0 \times 10^{-5}$ eV atom$^{-1}$, and the structure relaxation was conducted until the maximum force on each atom below 0.02 eV Å$^{-1}$.

The energy of adsorption for reaction intermediates was calculated as follows:

$$E_{\text{adsorption}} = E_{\text{t}} - E_a - E_b \quad (1)$$

where $E_{\text{t}}$ is the total energy of the adsorbed system, $E_a$ and $E_b$ represent the total energy of free species and bare surface, respectively.

The phase diagram of the discharge products is built based on the adsorption energy calculation. The SSLOB ORR/OER reaction free energy were determined by Norskov's calculation method.

*Computational simulations* the simulations were conducted on the COMSOL Multiphysics 6.0 software, and the operational details were shown in support information.

## 3 Results and Discussion

### 3.1 Activity Origins of HECs

To reveal the influence of local electronic structure in HECs on the catalytic conversion of $O_2/Li_2O_2$, a series of unitary $KMF_3$ (M = Co, Mn, Ni, Mg, Zn) and quinary $KCoMnNiMgZnF_3$-HEC models were established for DFT calculations (Fig. 1a, b). Electron localization functions (Fig. 1c-h,) and Bader charge (Table S1) elucidate the electron density redistribution of interfacial metal atoms in HEC, which modulates the *d*-band center, as evidenced by the projected density of states (PDOS, Fig. 1i). Figures 1j–s and S1 illustrate the diagrams of charge density difference for the $LiO_2$ adsorbed on different sites and the corresponding adsorption energy ($\Delta E_a$), in that the blue area and yellow area presents the lost electron and the gained electron, respectively. Clearly, abundant electron transfers occur on metal sites, manifesting the strong electronic interaction between reaction sites and $LiO_2$. It's worth noting that the Co*, Mn*, Ni*, Mg*, Zn* site in $KCoMnNiMgZnF_3$-HEC achieves more appealing $\Delta E_b$ of −2.59, −3.11, −1.40, −2.45, −2.83 eV, respectively, compared to those in $KMF_3$ candidates, enabling a moderate binding strength of $LiO_2$. In fact, the $O_2/Li_2O_2$ conversion in LOB system involves the *d*–*p* orbital hybridization between active site and key intermediate $LiO_2$. This interaction is related to the occupancy state of antibonding orbitals, which depends on the energy level of *d*-band, according to the *d*-band theory [8, 16, 17]. Since the antibonding states are always above the *d* states in terms of energy, the *d*-band center model would be a significant descriptor of the interaction between the catalyst and intermediate. Taking Co* adsorbed configuration as a representative, *d*-band center in HEC shows a slight upshift trend (Fig. 1i), implying the less filling of the antibonding states, leading to an elevated coupling of $LiO_2$ (Fig. 1j, o). Therefore, it is believed that the entropy effect manipulates the local electron configuration and the *d* orbital electron filling, which endows multiple metal active sites in $KCoMnNiMgZnF_3$-HEC with a favorable adsorbed energy of $LiO_2$.

To profoundly understand the ORR/OER thermodynamics on multiple sites in HEC, we established the phase diagram of possible intermediates ($Li_xO_y$, $x = 1$, $y = 2$; $x = 3$, $y = 4$) and discharge products (Fig. 1t–x). The adsorption energy calculation is defined as $\Delta E = \Delta E_0 + neU$, where $n$, $e$, and $U$ represents the charge transfer number, electron charge, and electrode potential, respectively [18]. The formation of $LiO_2$ is thermodynamically advantageous on Co*, Mn*, Ni*, Mg*, Zn* site when the discharge voltage is below 2.56, 3.08, 0.83, 2.43, 1.28 V, respectively. Notably, the $LiO_2$ can maintain stability on Mn* site at potentials greater than 1.80 V, while $Li_3O_4$ dominates at potentials greater than 1.92, 1.33, 1.14 V on Co*, Mg*, Zn* site, respectively. These results substantiate the ability of multiple sites in HEC for stabilizing $Li_{2-x}O_2$ intermediates. The difference ($\Delta U$) between minimum OER potential and maximum ORR potential (Fig. 1y), as a theoretical descriptor of catalytic activity, is predicted on the proposed models based on the Gibbs free energy of each endothermic step (Tables S2, S3). Apparently, Co*, Mn*, Ni*, Mg*, Zn* site in $KCoMnNiMgZnF_3$-HEC shows a


https://doi.org/10.1007/s40820-023-01275-3

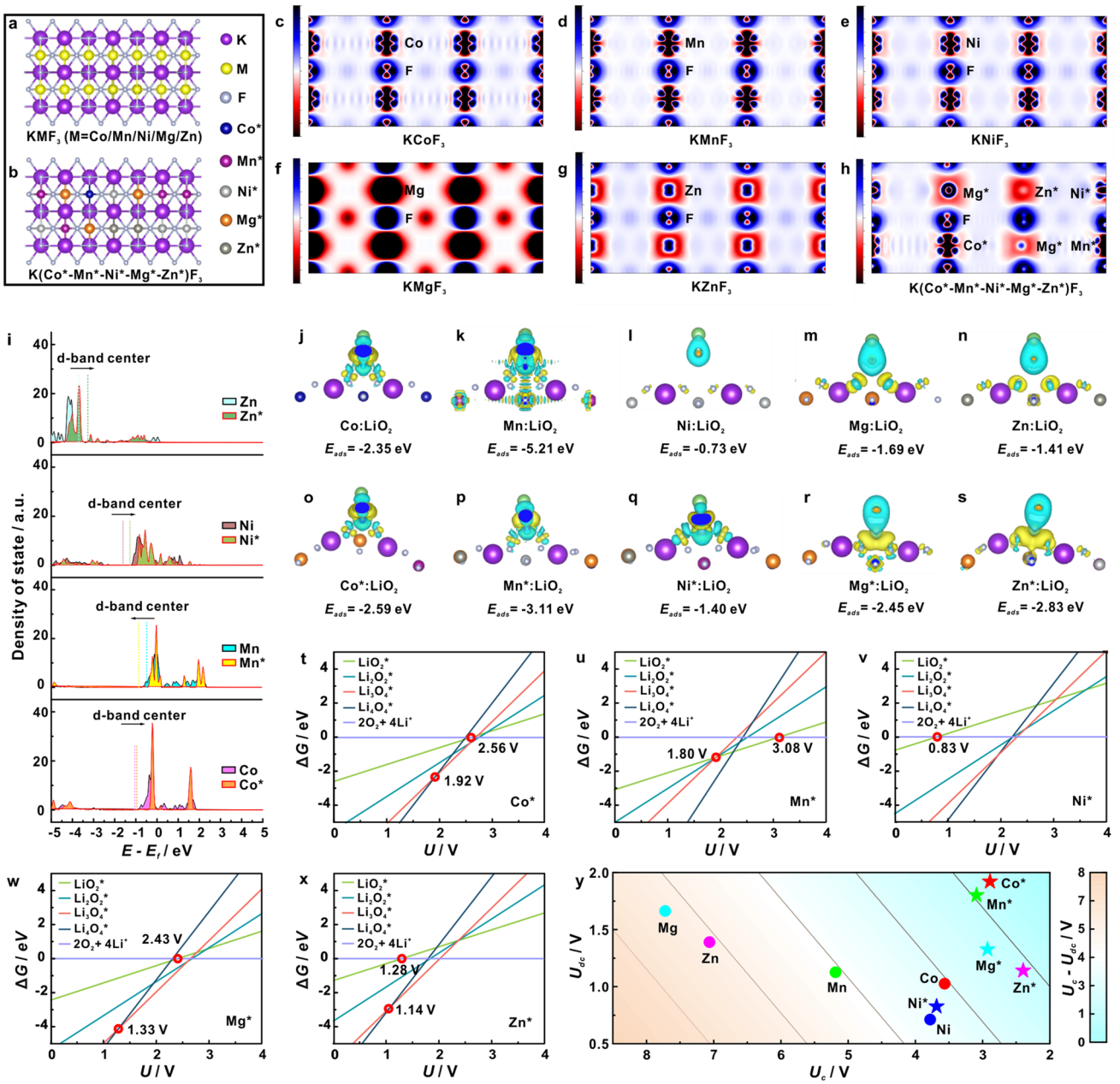


**Fig. 1** The optimized structural models of **a** $KMF_3$ and **b** $KCoMnNiMgZnF_3$-HEC. Cross-section of the charge density difference diagrams of **c** $KCoF_3$, **d** $KMnF_3$, **e** $KNiF_3$, **f** $KMgF_3$, **g** $KZnF_3$, **h** $KCoMnNiMgZnF_3$-HEC. **i** PDOS and corresponding calculated d-band centers of Co 3*d* in different models. Optimized structures and the corresponding binding energy of intermediate $LiO_2$ on the sites of **j** Co in $KCoF_3$, **k** Ni in $KNiF_3$, **l** Ni in $KNiF_3$, **m** Mg in $KMgF_3$, **n** Zn in $KZnF_3$, and **o** Co*, **p** Mn*, **q** Ni*, **r** Mg* and **s** Zn* in $KCoMnNiMgZnF_3$-HEC. The phase diagram of possible intermediates and discharge products on the sites of **t** Co*, **u** Mn*, **v** Ni*, **w** Mg* and **x** Zn* in $KCoMnNiMgZnF_3$-HEC. **y** The contours of predicted catalytic activity for different sites in various models

lower $\Delta U$ compared with that in $KMF_3$, suggesting the enhanced reaction kinetics. Therefore, the appropriate electronic environment of the $KCoMnNiMgZnF_3$-HEC triggered by entropy effect can realize the multi-active sites for moderate adsorption of key intermediates during the electrocatalysis, which maximizes the utilization of surface electroactivity, dramatically optimizing the reaction pathway.

### 3.2 Synthesis and Structural Characterization

Inspired by the highlighted catalytic activity of $KCoMnNiMgZnF_3$-HEC, we would like to shed light on the essentials of synergistic regulation mechanisms in HEC. Based on the DFT prediction, the model electrocatalysts, $KCoF_3$, $KCoMnNiF_3$, $KCoMnNiMgF_3$, $KCoMnNiZnF_3$, $KCoMnNiMgZnF_3$-HEC were experimentally prepared through a one-pot solvothermal route, as illustrated in Fig. 2a–d. In XRD patterns with detailed Rietveld refinements (Fig. 2e), the $KCoMnNiMgZnF_3$-HEC shares the same characteristics to that of $KCoF_3$, suggesting the cubic perovskite structures. Obviously, the diffraction peak originating from the (110) plane slightly shift to lower angles after changing in the numbers of elements, demonstrating a strong high-entropy effect. The SEM and TEM images (Figs. 2f, i and S2) exhibit a uniform cubic shape with an average size of 20 nm. The lattice fringe spacing of 0.288 and 0.292 nm can be assigned to (110) planes of $KCoF_3$ (Figs. 2g and S3a) and $KCoMnNiMgZnF_3$-HEC (Figs. 2j and S3b), respectively, in good consistent with the XRD results. The inductively coupled plasma-optical emission spectrometer (ICP-OES, Table S4) determines the chemical formula of $K_{0.95}Co_{0.24}Mn_{0.20}Ni_{0.22}Mg_{0.18}Zn_{0.16}F_{3.05}$. The corresponding fast Fourier transform (FFT) patterns (Fig. 2h, k) further confirm the single crystal structures of the products. Energy dispersive X-ray spectroscopy (EDS) mapping images (Fig. 2l, m) present the highly homogeneous elemental distribution, validating the complete formation of single-phase $KCoMnNiMgZnF_3$-HEC.

The XPS was carried out to investigate the chemical states and electronic effects of $KCoMnNiMgZnF_3$-HEC. Figure S4 demonstrates the presence of these Co, Mn, Ni, Mg, and Zn elements in $KCoMnNiMgZnF_3$-HEC. From the Co 2*p* spectrum (Figs. 3a and S5), the main peaks at 780.0, 796.4, 782.2, 798.6, 786.3 and 802.7 eV correspond to $Co^{3+}$ $2p_{3/2}$, $Co^{3+}$ $2p_{1/2}$, $Co^{2+}$ $2p_{3/2}$, $Co^{2+}$ $2p_{1/2}$, Co Sat. $2p_{3/2}$, Co Sat. $2p_{1/2}$, respectively [19]. Compared with $KCoF_3$, Co* in $KCoMnNiF_3$, $KCoMnNiMgF_3$, $KCoMnNiZnF_3$, $KCoMnNiMgZnF_3$-HEC show negative shifts, indicating the electron donating nature. In comparison, the electron interaction in HEC is most moderate as evidenced by a very minor variation in binding energy. To determine the spin polarization regulation of the as-prepared $KCoMnNiMgZnF_3$-HEC, the electron paramagnetic resonance (EPR) spectroscopy was carried out. The major characteristic signals with a *g*-factor of 2.037 (Eq. S1) correspond to the spin Co, Mn, Ni, Mg, Zn species were detected (Figs. 3b and S6), manifesting the presence of unpaired electrons. Meanwhile, the X-ray absorption spectroscopy (XAS) was performed to understand the critical role of high-entropy effect in manipulating the electronic structure of $KCoMnNiMgZnF_3$-HEC. X-ray absorption near edge structure (XANES) spectra of Co K-edge (Fig. 3c) reveal a positive oxidation state of $Co^{2+}$ in $KCoF_3$ and $KCoMnNiMgZnF_3$-HEC. In contrast with $KCoF_3$, the peak of derivative XANES of $KCoMnNiMgZnF_3$-HEC (Fig. 3d) was shifted to high energy, implying the higher valence state of Co, consistent with the XPS analysis results. In the Fourier-transformed EXAFS spectra (Fig. 3e), $KCoMnNiMgZnF_3$-HEC presents only one main peak at ca. 1.65 Å, corresponding to the combined Co-F coordination [20]. This coordination path can be better visualized by the maxima in the wavelet transform (WT) of the EXAFS (Fig. 3f), which is quite different compared to that of Co foil, CoO and $Co_3O_4$. We therefore conclude that the high-entropy effect can modulate the chemical environment and local structure, facilitating the 3*d* electron redistribution and further optimizes *d-p* orbital hybridization during electrocatalysis process.

### 3.3 Evaluation of Electrochemical Performance

To make comprehensive analysis of the structure-performance relationship for multi-sites electrocatalyst, the electrocatalytic properties of the as-prepared electrocatalysts were evaluated in a LOB system (Fig. 4a). Figure 4b depicts the first discharge–charge voltage curves at a current density of 500 mA $g^{-1}$ under an upper-limit capacity of 1000 mAh $g^{-1}$. It is evident that the $KCoMnNiMgZnF_3$-HEC cathode displays the smallest discharge–charge polarization (0.24/0.46 V), far lower than that of other candidates, illustrating the synergetic action among multiple sites on reaction kinetics of $O_2/Li_2O_2$ conversion. The corresponding details of ORR process can be visualized in Fig. 4c. In deep discharge–charge process (Fig. 4d), the $KCoMnNiMgZnF_3$-HEC cathode delivers an exceptionally high discharge specific capacity of 22,104 mAh $g^{-1}$ at current density of 200 mA $g^{-1}$, much superior to that of $KCoF_3$ (6710 mAh $g^{-1}$), $KCoMnNiF_3$ (7574 mAh $g^{-1}$), $KCoMnNiMgF_3$ (12,423 mAh $g^{-1}$) and $KCoMnNiZnF_3$ (17,482 mAh $g^{-1}$). Significantly, the

 https://doi.org/10.1007/s40820-023-01275-3

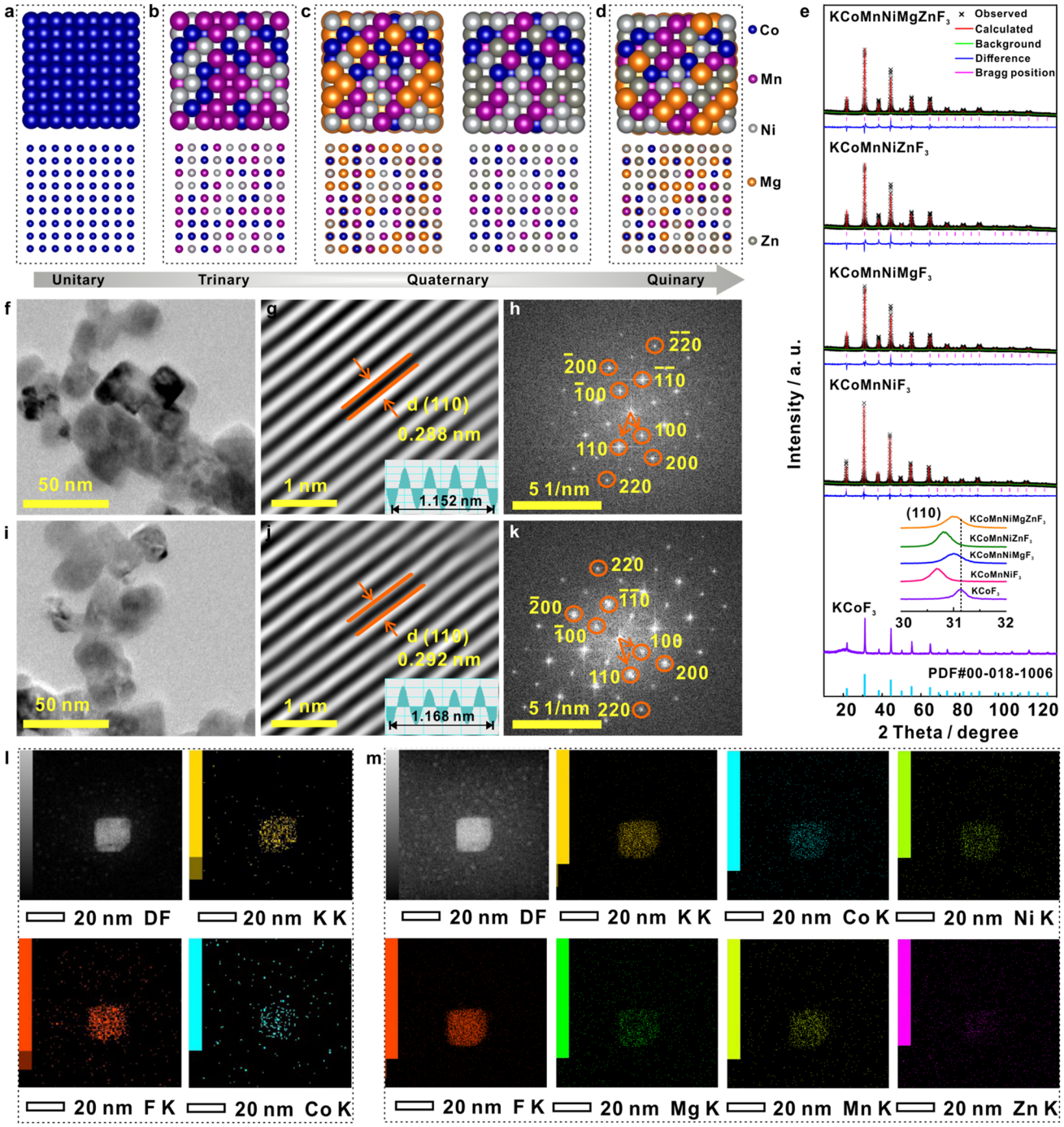


**Fig. 2** The structural schematic diagram perovskite fluorides for **a** unitary, **b** trinary, **c** quaternary and **d** quinary. **e** XRD patterns of $KCoF_3$, $KCoMnNiF_3$, $KCoMnNiMgF_3$, $KCoMnNiZnF_3$ and $KCoMnNiMgZnF_3$-HEC with detailed rietveld refinements. TEM (**f**), the inversed fast Fourier transform (IFFT) image (**g**), and FFT pattern (**h**) of $KCoF_3$. TEM (**i**), the IFFT image (**j**) and FFT pattern (**k**) of $KCoMnNiMgZnF_3$-HEC. EDS mapping of **l** $KCoF_3$ and **m** $KCoMnNiMgZnF_3$-HEC

$KCoMnNiMgZnF_3$-HEC cathode can maintain its higher capacity retentions and coulombic efficiencies than the other counterparts even at a current density of 400, 800 and 1000 mA $g^{-1}$ (Figs. 4e and S7-S11, Table S5), which corroborates prominent advantage of $KCoMnNiMgZnF_3$-HEC in boosting electrochemical performance. Electrochemical

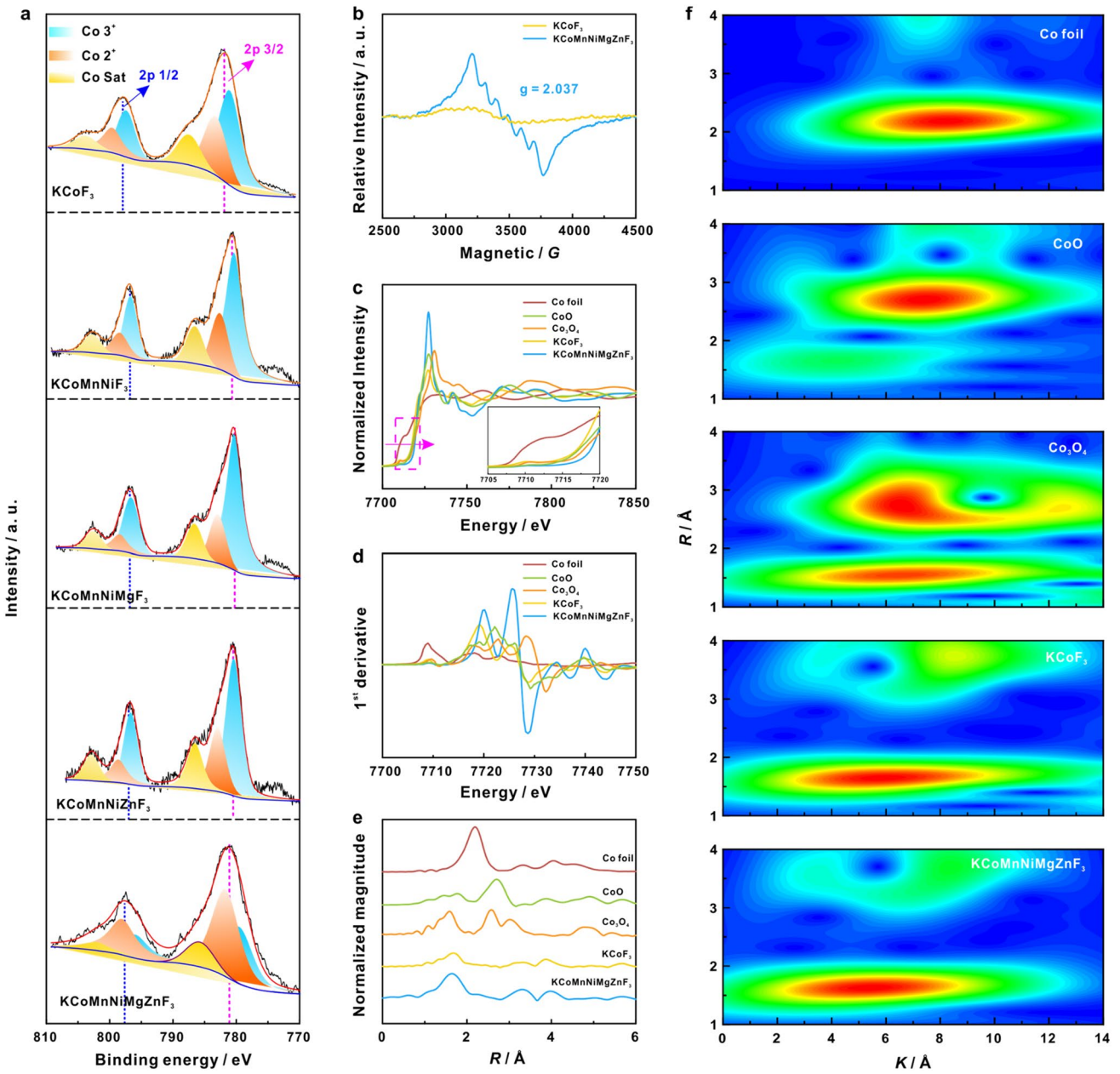


**Fig. 3** **a** High-resolution Co 2*p* XPS spectra of $KCoF_3$, $KCoMnNiF_3$, $KCoMnNiMgF_3$, $KCoMnNiZnF_3$ and $KCoMnNiMgZnF_3$-HEC. **b** EPR spectra of $KCoF_3$ and $KCoMnNiMgZnF_3$-HEC, **c** XANES spectra, **d** first derivatives of XANES and **e** Fourier transformed EXAFS for Co foil, $Co_3O_4$, $KCoF_3$, $KCoMnNiMgZnF_3$-HEC, and **f** the corresponding WT contour plots

impedance spectra (EIS) were performed to survey the reversibility of LOB. As depicted in Fig. S12 (Table S6), the $KCoMnNiMgZnF_3$-HEC-based LOB exhibits a low charge transfer resistance ($R_{ct}$) at full discharging, indicating a rapid charge transfer process at the three-phase interface of cathode-electrolyte-$Li_2O_2$. Upon recharging, the $KCoMnNiMgZnF_3$-HEC-based LOB almost fully recovers to its initial state, which stands in stark contrast to that of $KCoF_3$ and highlights its exceptional reversibility.

The cycle life as another critical parameter is measured by long-term discharge/charge test. As revealed in Fig. 4f, the $KCoMnNiMgZnF_3$-HEC based LOB achieves a long cycle lifetime of 1000 h (500 cycles) at a high current density of 1000 mA $g^{-1}$ with a limited capacity of 1000 mAh $g^{-1}$, 1.3,


https://doi.org/10.1007/s40820-023-01275-3

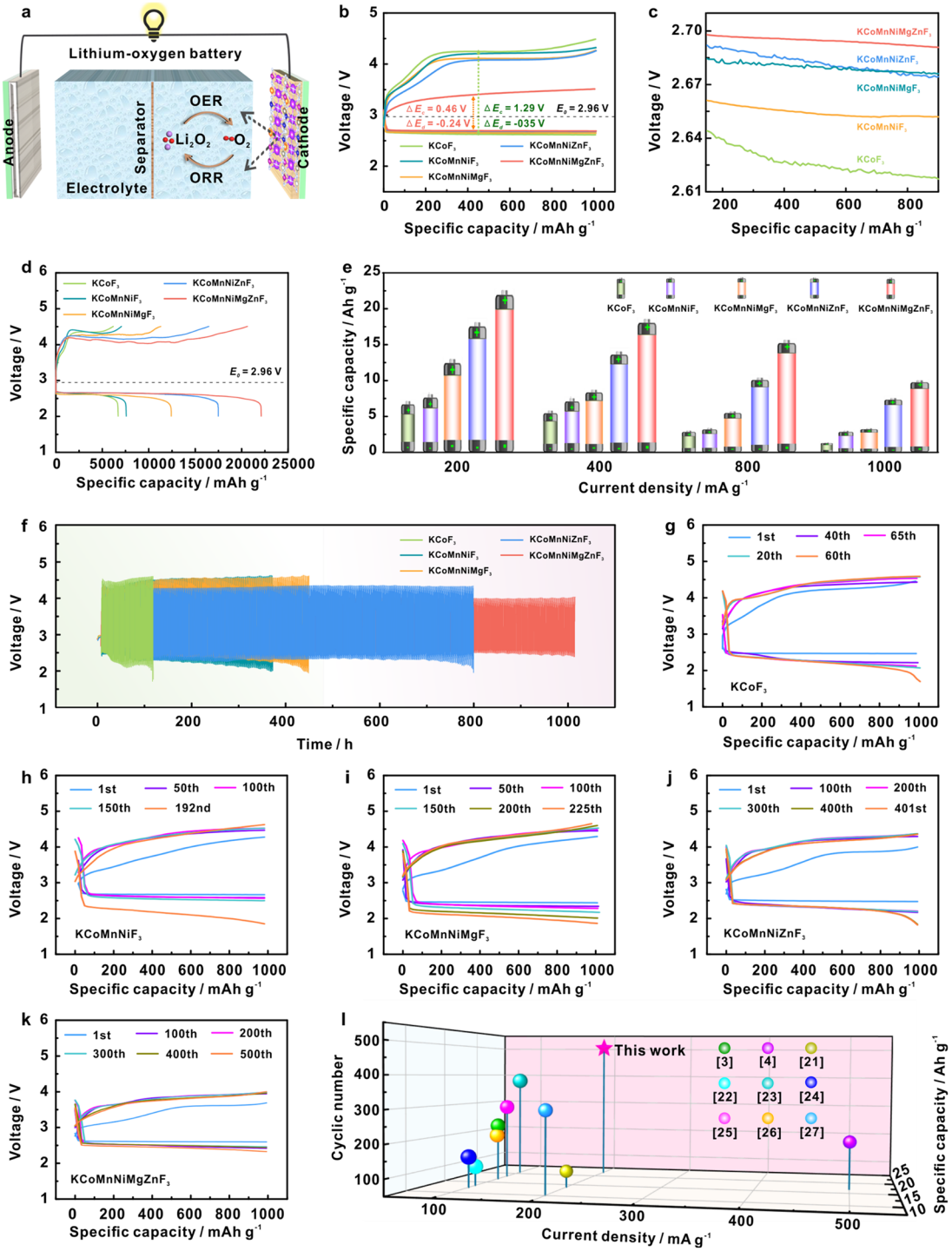


**Fig. 4** **a** Schematic of a LOB and ORR/OER reaction mechanism. **b** The first discharge–charge voltage curves at a current density of 500 mA $g^{-1}$ under an upper-limit capacity of 1000 mAh $g^{-1}$, and **c** the corresponding details of the selected region in (**b**), **d** the first galvanostatic discharge/charge curves at a current density of 200 mA $g^{-1}$ between 2.0 and 4.5 V, **e** discharge capacities at various current densities, **f** the cycle stability and **g–k** the corresponding galvanostatic discharge/charge curves extracted from whole cycling of the Li–$O_2$ cells with $KCoF_3$, $KCoMnNiF_3$, $KCoMnNiMgF_3$, $KCoMnNiZnF_3$, and $KCoMnNiMgZnF_3$-HEC. **l** Performance comparisons (capacity and cycle stability) of $KCoMnNiMgZnF_3$-HEC and other representative published efforts

2.2, 2.6, 8.3 times higher than that of $KCoF_3$, $KCoMnNiF_3$, $KCoMnNiMgF_3$, and $KCoMnNiZnF_3$, respectively. Figure 4g–k presents the corresponding discharge–charge curves of those candidates during long cycling. It is apparent that the $KCoMnNiMgZnF_3$-HEC cathode remains a relatively lower overpotential over long periods, demonstrating extraordinary reversibility. As a result, the notorious parasitic reactions from electrolyte degradation and catalyst poisoning can be effectively suppressed, which contributes to the enhancement of round-trip efficiency and reversibility for LOB. Combining previous theoretical simulations (Fig. 1) and experimental determinations (Fig. 3), the excellent electrochemical performance of $KCoMnNiMgZnF_3$-HEC can be attributed to the synergetic action among multiple sites, in which the entropy effect engenders an increased population of unpaired electrons, leading to the electron rearrangement with an elevated spin polarization, dramatically optimizing the *d-p* orbital hybridization between cation sites and key intermediate. To our knowledge, those performance parameters of the LOB with $KCoMnNiMgZnF_3$-HEC precede majority of traditional catalysts reported in previous studies (Fig. 4l and Table S7) [3, 4, 21–27].

### 3.4 Evolution of Cathodes Products during Discharge and Charge Process

Inspired by the impressive electrochemical performance of $KCoMnNiMgZnF_3$-HEC, the morphological evolution and chemical characteristics of cathodes products at various discharge stages was further investigated. Through observation on the SEM images (Fig. 5a–e), it is found that the grain-shaped products appear on those cathodes after discharged to 1000 mAh $g^{-1}$. As revealed in the date visualization (Fig. 5f–j), the distribution of products becomes more and more uniform as the number of metallic elements increment in catalyst, suggesting that the multiple active sites in HEC are capable of promoting the homogeneous nucleation of products. After full discharging, the products on the $KCoF_3$ (Fig. 5k, p) and $KCoMnNiF_3$ (Fig. 5l, q) cathodes evolve into a closely packed amorphous morphology, which can be identified as $Li_2O_2$ and $Li_2CO_3$ by high-resolution XPS analysis (Fig. 5u, v). In stark contrast, toroidal $Li_2O_2$ accommodations are deposited evenly on the $KCoMnNiMgF_3$ (Fig. 5m, r), $KCoMnNiZnF_3$ (Fig. 5n, s) and $KCoMnNiMgZnF_3$-HEC (Fig. 5o, t) cathode with the absence of obvious signal of $Li_2CO_3$ (Fig. 5w–y). It is worth mentioning that the order degree of cathode products correlated strongly with the number of atomic species in catalyst, verifying the modulating effect of the exposed multiple active sites in HEC on the growth pathway of $Li_2O_2$ (Schematic diagram in Fig. 5z). Essentially speaking, the $Li_2O_2$ morphology and structure are the most important indexes in dominating LOB performance, including overpotential, capacity, cyclability, etc., while the $Li_2O_2$ formation mechanism is influenced by the adsorption behavior of key intermediates, which is closely relevant to the *d–p* orbital hybridization between catalyst and $LiO_2$. In combination with DFT calculations (Fig. 1i–s), it is reasonable to deduce that mixed elements in $KCoMnNiMgZnF_3$-HEC engender significant 3*d* charge redistribution and create multiple active sites with optimized energy barriers for stabilizing $LiO_2$ intermediates, which dramatically improves the electrochemical performance of LOB.

To thoroughly elucidate the relationship between the $Li_2O_2$ growth model and the electrochemistry toward ORR kinetics, the $Li_2O_2$ deposition behavior on $O_2$-electrode was simulated using COMSOL Multiphysics (Fig. S13, Table S8) [28]. Based on Kolmogrov's phase transformation theory [29] and Sampson and Lynden models [30] combined with experimental results, two 2D transient matrixes were constructed (Figs. S14 and S15). Figure 6a displays the contours of $O_2$ concentration distributions and $Li_2O_2$ porosity on $O_2$-electrode at different discharge stages, where the heterogeneous nucleation of $Li_2O_2$ on $KCoF_3$ cathode donates as model I and homogeneous nucleation of $Li_2O_2$ $KCoMnNiMgZnF_3$-HEC cathode donates as model II, taking the previously obtained SEM characterizations (Figs. 5a, k, e, o) as evidence. It is clear that the $O_2$ transfer kinetics slows down with the increase of depth of discharge (DOD), which is attributed to the clogging of porous $O_2$-electrode due to the accumulation of $Li_2O_2$. We therefore speculate that the formation of $O_2$ "dead zone" in cathode was the most common cause of LOB failure. In fact, the accumulation of discharge products on $O_2$-electrode cuts off the $O_2$-electrode-eletrolyte interaction, which greatly discounts the efficiency of electron and mass transfer, resulting in a constantly-increasing polarization. Videos S1 and S2 exhibited the animate simulations of model I and model II, respectively. From the comparison, the $O_2$ diffusion depth, $O_2$ concentration (Fig. 6b, c), cathode porosity (Fig. 6d, e) and $Li_2O_2$ porosity (Fig. 6f, g) on model II were significantly

 https://doi.org/10.1007/s40820-023-01275-3

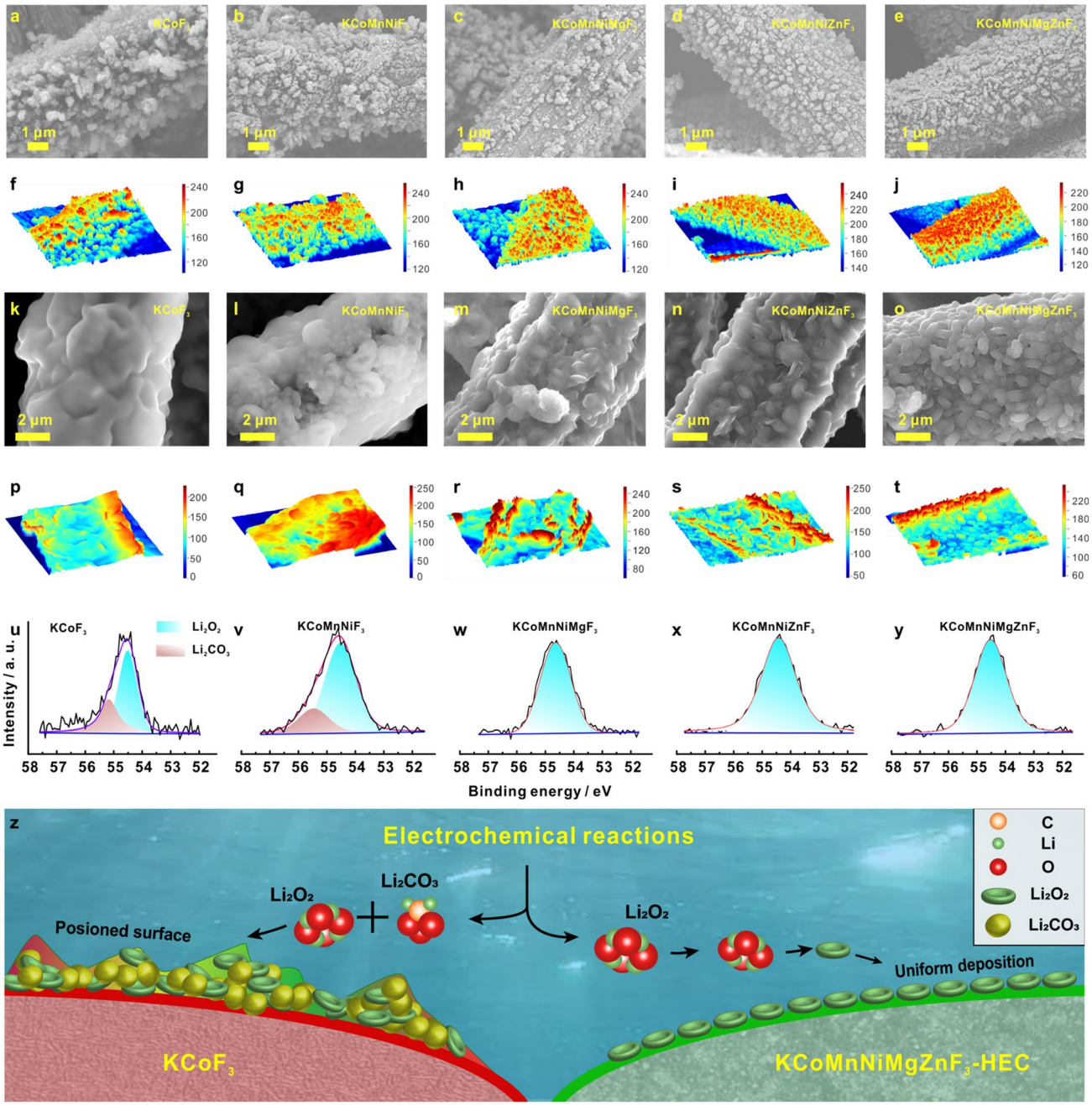


**Fig. 5** SEM images of cathodes after discharged to 1000 mA h $g^{-1}$ at a current density of 500 mA $g.^{-1}$ with **a** $KCoF_3$, **b** $KCoMnNiF_3$, **c** $KCoMnNiMgF_3$, **d** $KCoMnNiZnF_3$, **e** $KCoMnNiMgZnF_3$-HEC, and **f–j** The corresponding date visualization. SEM images of cathodes after full discharge with **k** $KCoF_3$, **l** $KCoMnNiF_3$, **m** $KCoMnNiMgF_3$, **n** $KCoMnNiZnF_3$, **o** $KCoMnNiMgZnF_3$-HEC, and **p–t** The corresponding date visualization. High-resolution Li 1*s* XPS spectra of cathodes after full discharge with **u** $KCoF_3$, **v** $KCoMnNiF_3$, **w** $KCoMnNiMgF_3$, **x** $KCoMnNiZnF_3$, **y** $KCoMnNiMgZnF_3$-HEC. **z** Schematic illustration of discharge reaction mechanisms on $KCoF_3$ (lift) and $KCoMnNiMgZnF_3$-HEC (right)

higher than that of model I, suggesting that the homogeneous deposition of $Li_2O_2$ triggered by multiple active sites in $KCoMnNiMgZnF_3$-HEC can enhance the mass transfer at the three-phase interface among gas-$Li_2O_2$-electrolyte, and thereby alleviating the passivation of $O_2$-electrode. Under such circumstance, the LOB enables a fast reaction kinetics, which holds attractive electrochemical performance, well consistent with simulated results (Fig. S16).

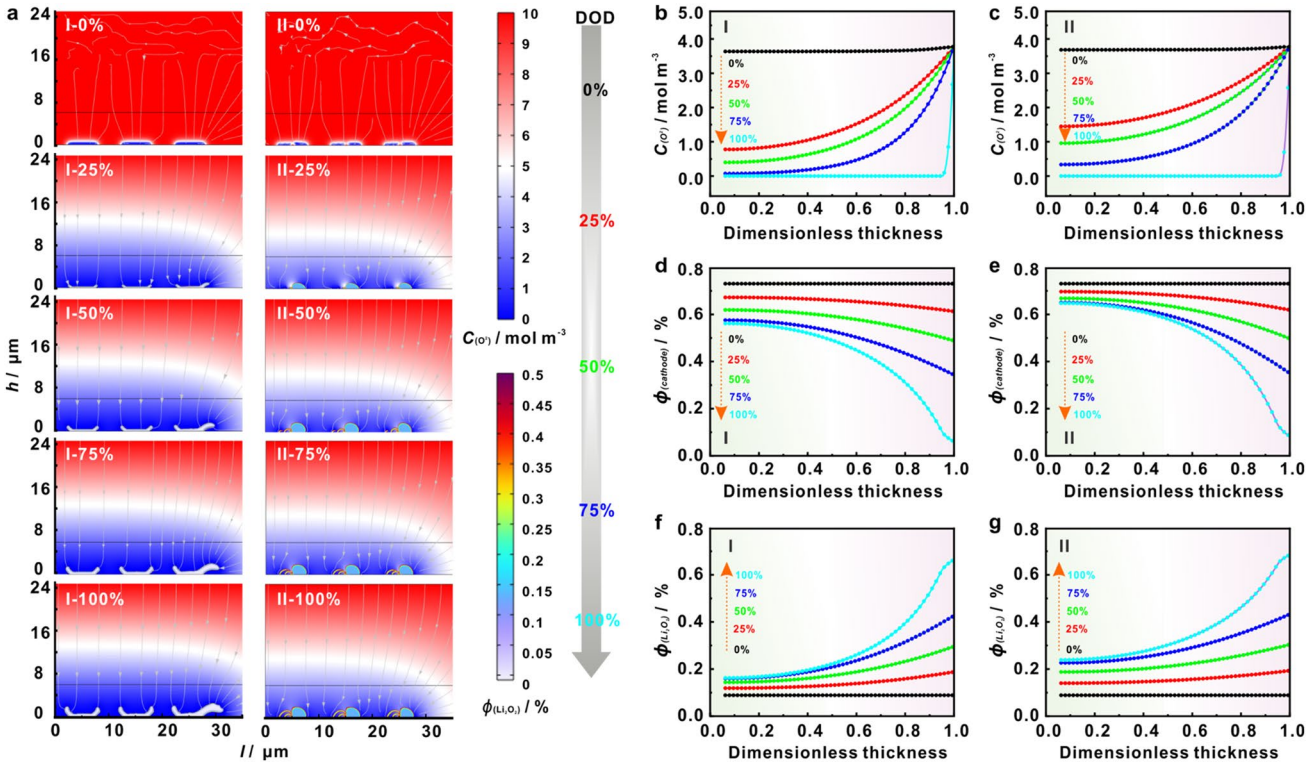


**Fig. 6** COMSOL simulations of $Li_2O_2$ growth kinetics on cathodes with $KCoF_3$ (model I) and $KCoMnNiMgZnF_3$-HEC (model II) for **a** $O_2$ concentration distributions and $Li_2O_2$ porosity at different discharge stages (0% DOD, 25% DOD, 75% DOD, 100% DOD), **b** and **c** the corresponding curves of $O_2$ concentration distributions, **d** and **e** cathode porosity and **f** and **g** $Li_2O_2$ porosity

### 3.5 Function of Entropy Effect on Enhanced Cyclic Performance

Further investigations were centered on the reversibility of those kinds of cathode. To identify the cathode surface condition, the cycled LOBs were disassembled and analyzed. XRD (Fig. 7a) and Raman patterns (Fig. 7b) reveal the formation of $Li_2CO_3$, LiOH, LiAc, and $LiRCO_3$ as main side-products on $KCoF_3$, $KCoMnNiF_3$, $KCoMnNiMgF_3$ and $KCoMnNiZnF_3$ cathode [31, 32]. In striking contrast, no signal peak assigned to those byproducts emerges on $KCoMnNiMgZnF_3$-HEC cathode, even after 500th cycles, unveiling the suppression effect of multiple active sites in HEC on side reactions. It is clear from Fig. 7c, d that accumulative products completely cover the $KCoF_3$ cathode after cycling. Since the attachment of those indissoluble products on cathode surface during cycling, catalytic active centers were gradually blocked, leading to a restricted electrochemistry and aggravated side reactions. In comparison, the $KCoMnNiMgZnF_3$-HEC cathode (Fig. 7e, f) basically maintains a fresh interface condition throughout the entire cycles, demonstrating the excellent anti-passivation power. Moreover, the cycled $KCoMnNiMgZnF_3$-HEC exhibits a superior preservation of its pristine structure compared to $KCoF_3$, as evidenced by Fig. S17, suggesting the excellent stability. Those results provide obvious proof of significant improvement on the long-term durability of LOB with $KCoMnNiMgZnF_3$-HEC catalyst. Accordingly, a schematic illustration of the cycling electrochemistry occurring on the $KCoF_3$ and $KCoMnNiMgZnF_3$-HEC cathode is demonstrated in Fig. 7g.

To determine the reaction pathway and conversion kinetics, high-resolution ex-situ XPS techniques were conducted on the $KCoMnNiMgZnF_3$-HEC cathode at selected pivotal states (Fig. 7h). In the Li 1*s* spectra (Fig. 7i), the peaks around 55.9 and 54.8 eV can be assigned to $Li_{2-x}O_2$ and $Li_2O_2$, respectively. At the beginning of discharge (stage I), the signals of $Li_{2-x}O_2$ and $Li_2O_2$ appeared in the Li 1*s* spectrum, certifying a multi-step process of ORR. As the discharge proceeded, the ratio of $Li_{2-x}O_2$ / $Li_2O_2$ decreased significantly (stage II), indicating the transformation of $Li_{2-x}O_2$ intermediate into $Li_2O_2$ product. Therefore, the

 https://doi.org/10.1007/s40820-023-01275-3

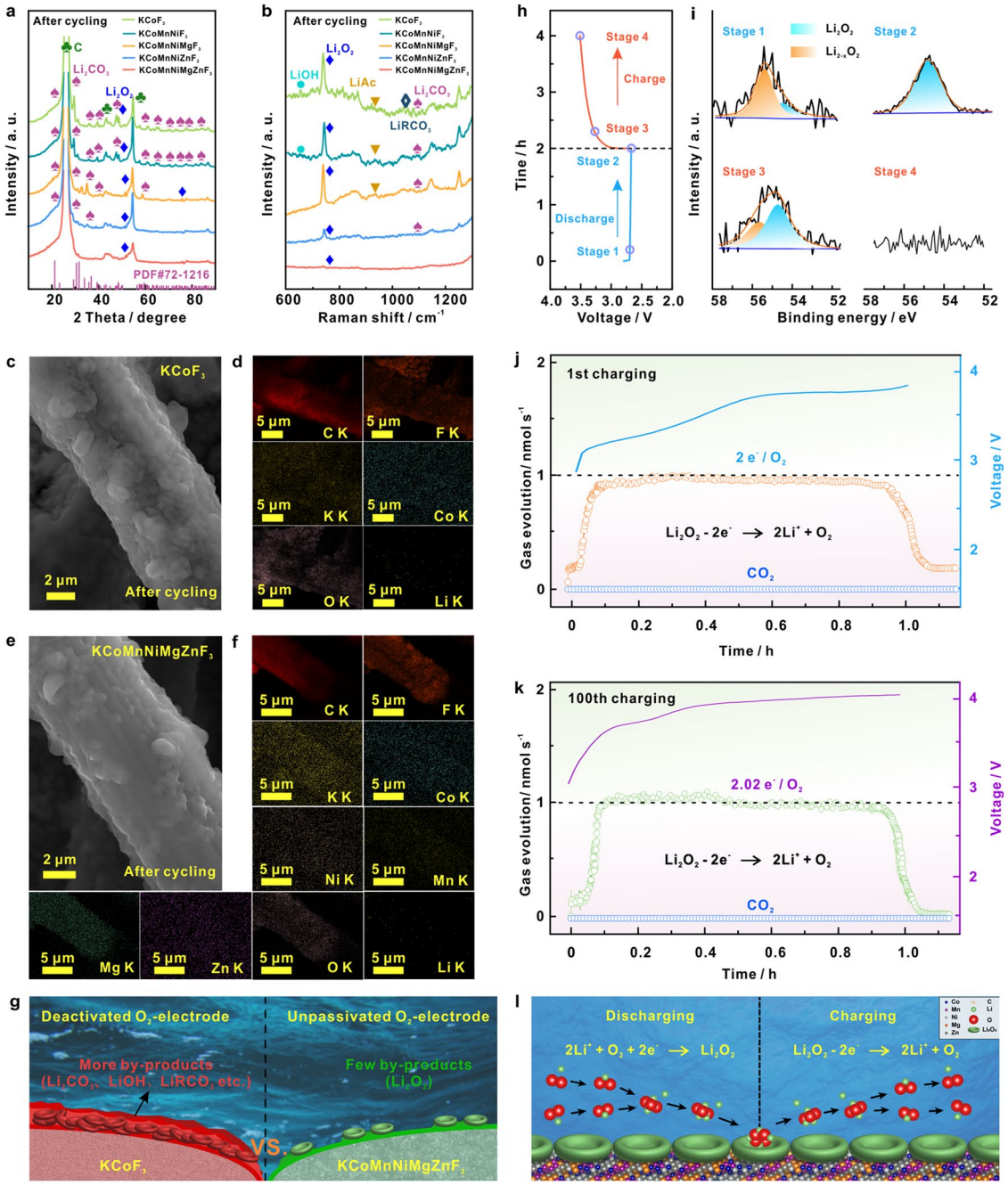


**Fig. 7** a XRD, and **b** Raman spectra of cathodes with $KCoF_3$, $KCoMnNiF_3$, $KCoMnNiMgF_3$, $KCoMnNiZnF_3$, $KCoMnNiMgZnF_3$-HEC after cycling at a current density of 1000 mA $g^{-1}$ under an upper-limit capacity of 1000 mAh $g^{-1}$. **c** SEM images and **d** EDS mapping of cathodes after cycling with $KCoF_3$. **e** SEM images and **f** EDS mapping of cathodes after cycling with $KCoMnNiMgZnF_3$-HEC. **g** Schematic illustration of cycling electrochemistry on $KCoF_3$ (lift) and $KCoMnNiMgZnF_3$-HEC (right). **h** Galvanostatic discharge–charge curves of the $KCoMnNiMgZnF_3$-HEC electrode at a current of 500 mA $g^{-1}$ with an upper-limit capacity of 1000 mAh $g^{-1}$, and **i** high-resolution XPS spectra of Li 1*s* at selected pivotal states as indexed in (**h**). In-situ DEMS curves of LOB with $KCoMnNiMgZnF_3$-HEC during charging process for **j** 1st cycling, **k** 100th cycling. **l** Schematic illustration of ORR/OER reaction mechanisms on $KCoMnNiMgZnF_3$-HEC cathode

possible ORR process on $KCoMnNiMgZnF_3$-HEC cathode can be described by the following Eqs. (2–4):

$$O_2 + e^- + Li^+ \rightarrow LiO_2^* \quad (2)$$

$$2LiO_2^* \rightarrow Li_2O_2 + O_2 \quad (3)$$

$$LiO_2* + e^- + Li^+ \rightarrow Li_2O_2^* \quad (4)$$

When recharged to state III, the intermediate $Li_{2-x}O_2$ reappears on $KCoMnNiMgZnF_3$-HEC cathode, implying the delithium process of $Li_2O_2$. At the final stage of recharging, the absence of Li 1*s* peak presents the complete decomposition of $Li_2O_2$. The results verify the ability to stabilize key intermediates on multiple active sites in $KCoMnNiMgZnF_3$-HEC cathode.

Moreover, the underlying reaction kinetics was analyzed with the assistance of in-situ differential electrochemical mass spectrometry (DEMS). The ratio of $2e^-/O_2$ on $KCoMnNiMgZnF_3$-HEC cathode was displayed in Fig. S18 (Eq. S2), supporting the discharging mechanism involving the reduction of $O_2$ along the two-electron pathway ($O_2 + 2Li^+ + 2e^- \rightarrow Li_2O_2$) [33]. Notably, during charging process, the oxidation processes were predominantly governed by oxygen releasement, as evidenced by the ratio of $2e^-/O_2$ in Fig. 7j, suggesting the electrochemical decomposition of $Li_2O_2$ ($Li_2O_2* - 2e^- \rightarrow 2\,Li^+ + O_2$), without involvement of other side reactions, aligning well with the XRD (Fig. 7a) and Raman (Fig. 7b) results. Due to the stabilization of intermediates on $KCoMnNiMgZnF_3$-HEC cathode, two-electron transfer can be achieved most effectively during ORR/OER process, which is of vital importance in boosting reaction kinetics. Encouragingly, the gas analysis plots of $O_2$ evolution maintained well in the 100th cycles (Fig. 7k), where the ratio of $v(e^-)$: $v(O_2)$ is determined as 2.02:1, manifesting considerable reversibility of $Li_2O_2$ formation/decomposition on $KCoMnNiMgZnF_3$-HEC cathode during long-term cycling. We speculate that the improvement of the durability of LOB is closely correlated to the modulation effect of multiple active sites on the reaction pathway, as illustrated in Fig. 7l.

### 3.6 Modulation Mechanism of Entropy Effect on Catalytic Kinetics

To in-depth shed light on the modulation mechanism of entropy effect on catalytic kinetics, we further carried out the DFT simulation and analysis. The local electron configurations of Co* site in $KCoF_3$, $KCoMnNiF_3$, $KCoMnNiMgF_3$ $KCoMnNiZnF_3$ and $KCoMnNiMgZnF_3$-HEC were first examined through the PDOS calculations. The Co* 3*d* PDOS (Fig. 8a) reveals the rearrangement of 3*d* orbital ($d_{xz/xy/yz}$, $d_{x^2-y^2}$, $d_{z^2}$) electron in both spin channels after introducing more metallic elements, signifying the strong interactions among elements. Especially, the $d_{x^2-y^2}$ and $d_{z^2}$ in $KCoMnNiMgZnF_3$-HEC leap into Fermi energy level compared to that of $KCoF_3$, demonstrating the electron transition from low-energy orbitals to high-energy orbitals [34–36]. Combined with the calculation of *g*-factor (Fig. 3b), it can be concluded that the local charge redistribution increases the unpaired electron density in $d_{xz/xy/yz}$ orbitals, enabling the alteration in the spin polarization. The difference charge density maps (the insets of Fig. 8a) present more electrons transfer of Co* in $KCoMnNiMgZnF_3$ than that of $KCoF_3$, which points to a higher positive valence of Co* in HEC, well consistent with XANES results (Fig. 3c, d). Based on the calculated electron spin states (Tables S9–S13), the possible electron arrangements of Co* in all those candidates were identified, as illustrated in Fig. 8b. Considering the moderate spin polarization of active sites in $KCoMnNiMgZnF_3$-HEC, it is believed that the adsorption of key intermediates in $O_2/Li_2O_2$ conversion can be greatly optimized (Figs. 1j, o and S19), thus bringing about an enhanced intrinsic activity. Base on hybrid orbital theory, the orbital interactions between Co* centers and $LiO_2$ intermediate were further discussed. As revealed by Fig. 8c, the $d_{xz/xy/yz}$ orbitals in $KCoMnNiMgZnF_3$-HEC match better with the 2*p* orbital of adsorbed $LiO_2$ in contrast with that of other counterparts, unveiling the optimal *d*-*p* orbital hybridization between HEC and intermediate. Due to the 3*d* orbital coupling of Co* in $KCoMnNiMgZnF_3$-HEC, the electron delocalization decreased the $d_{xz/xy/yz}$ orbitals energy level, which enables easier electron injection from the Co* $d_{xz/xy/yz}$ orbitals into O 2*p* orbital of $LiO_2$, thereby facilitating the conversion kinetics. On this basis, the *d*–*p* orbital hybridization during ORR process is visualized in Fig. 8d. In detail, the antibonding orbitals induced by the coupling between O 2*p* and Co* 3*d* located below the Fermi level. Owing to the entropy effect in $KCoMnNiMgZnF_3$-HEC, the Co* site denotes a higher *d*-band center and the electron donating nature, which engenders a favorable binding interaction between key intermediate $LiO_2$ and Co* site, reinforcing the intrinsic reaction activity.


https://doi.org/10.1007/s40820-023-01275-3

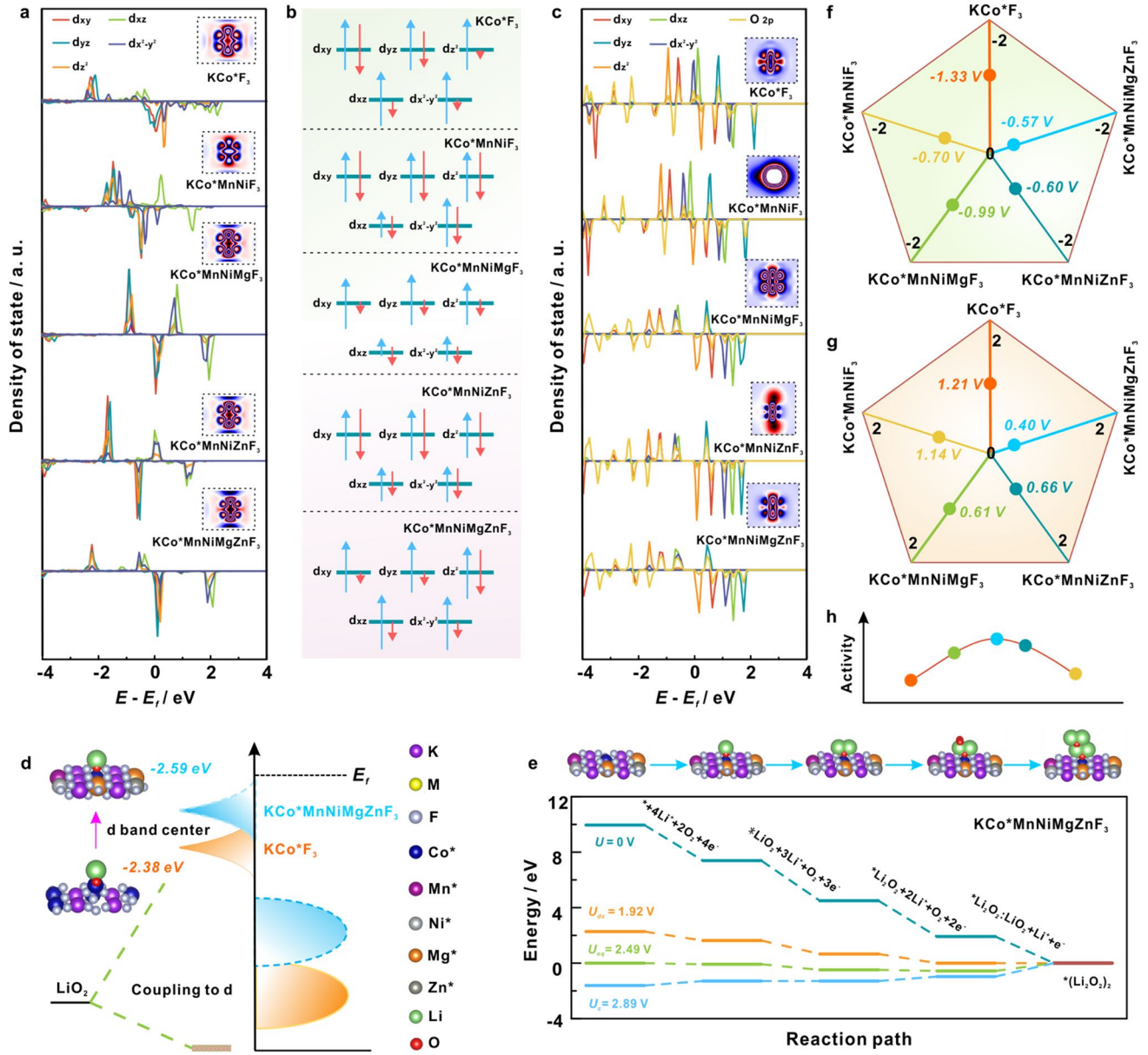


**Fig. 8** **a** PDOS of Co* 3*d* orbitals, and **b** Schematic diagrams of possible electron arrangements on 3*d* orbital, and **c** PDOS of O 2*p* orbitals for adsorbed $LiO_2$ and 3*d* orbitals of Co* centers in $KCoF_3$, $KCoMnNiF_3$, $KCoMnNiMgF_3$, $KCoMnNiZnF_3$, $KCoMnNiMgZnF_3$-HEC. **d** Schematic illustration of *d*–*p* orbital hybridization during ORR process on Co* site in $KCoF_3$ and $KCoMnNiMgZnF_3$-HEC. **e** Gibbs free energy diagram of ORR process on Co* site in $KCoMnNiMgZnF_3$-HEC. Comparison of **f** ORR overpotentials, **g** OER overpotentials, and **h** catalytic activity among $KCoF_3$, $KCoMnNiF_3$, $KCoMnNiMgF_3$, $KCoMnNiZnF_3$, $KCoMnNiMgZnF_3$-HEC

Figures S19a–d and 8e picturizes the reaction pathways toward the formation of $(Li_2O_2)_2$ clusters at different overpotentials for the LOBs on Co* site in those various catalysts built on the calculated free energy (Table S14). The discharge and charge overpotentials were referred to evaluate the catalytic activity, defined as $\Delta U_{dc} = U_{dc} - U_{eq}$, $\Delta U_c = U_c - U_{eq}$, where $U_{dc}$, $U_{eq}$ and $U_c$ represents the highest discharge potential, equilibrium potential and the lowest charge potential, respectively. It is evident from Fig. 8f–g that the overpotential of $KCoMnNiMgZnF_3$-HEC ($\Delta U_{dc}/\Delta U_c = -0.57/0.40$ V) is relatively lower than that of $KCoF_3$ ($\Delta U_{dc}/\Delta U_c = -1.33/1.21$ V), $KCoMnNiF_3$ ($\Delta U_{dc}/\Delta U_c = -0.70/1.14$ V), $KCoMnNiMgF_3$ ($\Delta U_{dc}/\Delta U_c = -0.99/0.61$ V) and $KCoMnNiZnF_3$

($\Delta U_{dc}/\Delta U_c = -0.60/0.66$ V), marking the highest catalytic activity (Fig. 8h). Those DFT results elucidate the modulating effect of the exposed multiple active sites in $KCoMnNiMgZnF_3$-HEC on enhancing ORR/OER kinetics, which strongly corroborated the obtained experimental determinations.

## 4 Conclusions

In summary, guided by the DFT screening, we tailored an ideal $KCoMnNiMgZnF_3$-HEC catalyst to support the ORR and OER reactions for the development of high-performance LOBs. It is revealed that the entropy effect of multiple sites in $KCoMnNiMgZnF_3$-HEC triggers the appropriate regulation of 3*d* orbital structure, leading to a moderate hybridization with the *p* orbital of key intermediates. As a result, $KCoMnNiMgZnF_3$-HEC-based LOB exerts an ultrahigh discharge capacity and outstanding long-term cyclability with a lowered overpotentials. Accordingly, we may draw a logical conclusion that, the $KCoMnNiMgZnF_3$-HEC catalyst is, momentous to positively manipulate discharge/charge behavior of LOBs. This study demonstrates that the *d* orbital occupancy unidirectionally affects *d*–*p* orbital hybridization between intermediates and catalysts and determines the catalytic kinetics. Tuning the active centers with desirable electron distribution is able to improve the electrochemical performance of LOBs. These findings provide an in-depth understanding of the correlation between multiple active sites in HEC and reaction intermediates, bringing new horizon to the electron modulation and *d*-band center optimization for electrocatalyst.

Although our proposed high-entropy perovskite fluoride catalyst has shown promising results in LOB catalysis, further research is required to fully comprehend the relationship between structural engineering and the optimization of catalytic behaviors, specifically in identifying site function. Furthermore, there is a need to bridge the gap between experimental design and theoretical prediction to achieve seamless connections in the catalytic applications of HEC catalysts. From the long-term point of view, advanced synthesis strategy, high-throughput screening technology and nondestructive characterization are essential for the functionalization of HEC catalysts, both for catalytic purposes and beyond. Through these collaborative efforts, we believe that the materials science and catalysis communities can come together to explore new frontiers in the discovery and design of high-efficient HEC catalysts.

**Acknowledgements** P. G. acknowledges the financial support from the Youth Foundation of Shandong Natural Science Foundation (No. ZR2023OB230), National Natural Science Foundation (No. 22309035) and Double First-class Discipline Construction Fund Project of Harbin Institute of Technology at Weihai (No. 2023SYLHY11).

**Declarations**

**Conflict of interest** The authors declare no interest conflict. They have no known competing financial interests or personal relationships that could have appeared to influence the work reported in this paper.



**Supplementary Information** The online version contains supplementary material available at https://doi.org/10.1007/s40820-023-01275-3.

## References

1. D. Wang, X. Mu, P. He, H. Zhou, Materials for advanced Li–$O_2$ batteries: explorations, challenges and prospects. Mater. Today **26**, 87–99 (2019). https://doi.org/10.1016/j.mattod.2019.01.016
2. X. Wu, B. Niu, H. Zhang, Z. Li, H. Luo et al., Enhancing the reaction kinetics and reversibility of Li–$O_2$ batteries by multifunctional polymer additive. Adv. Energy Mater. **13**, 2203089 (2023). https://doi.org/10.1002/aenm.202203089
3. L. Ren, R. Zheng, D. Du, Y. Yan, M. He et al., Optimized orbital occupancy of transition metal in spinel Ni–Co oxides with heteroatom doping for aprotic Li–$O_2$ battery. Chem. Eng. J. **430**, 132977 (2022). https://doi.org/10.1016/j.cej.2021.132977
4. Q. Lv, Z. Zhu, Y. Ni, J. Geng, F. Li, Spin-State manipulation of two-dimensional metal–organic framework with enhanced metal–oxygen covalency for lithium–oxygen batteries. Angew. Chem. Int. Ed. **61**, e202114293 (2022). https://doi.org/10.1002/anie.202114293

5. Y. Zhou, Q. Gu, K. Yin, Y. Li, L. Tao et al., Engineering $e_g$ orbital occupancy of Pt with Au alloying enables reversible Li–$O_2$ batteries. Angew. Chem. Int. Ed. **61**, e202201416 (2022). https://doi.org/10.1002/ange.202201416
6. X. Li, G. Han, S. Lou, Z. Qiang, J. Zhu et al., Tailoring lithium-peroxide reaction kinetics with $CuN_2C_2$ single-atom moieties for lithium-oxygen batteries. Nano Energy **93**, 106810 (2022). https://doi.org/10.1016/j.nanoen.2021.106810
7. L. Song, W. Zhang, Y. Wang, X. Ge, L. Zou et al., Tuning lithium-peroxide formation and decomposition routes with single-atom catalysts for lithium-oxygen batteries. Nat. Commun. **11**, 2191 (2020). https://doi.org/10.1038/s41467-020-15712-z
8. Y. Zhou, K. Yin, Q. Gu, L. Tao, Y. Li et al., Lewis-acidic PtIr multipods enable high-performance Li–$O_2$ batteries. Angew. Chem. Int. Ed. **60**, 26592–26598 (2021). https://doi.org/10.1002/anie.202114067
9. S. Ke, W. Li, Y. Gu, J. Su, Y. Liu et al., Covalent organic frameworks with Ni-bis (dithiolene) and Co-porphyrin units as bifunctional catalysts for Li–$O_2$. Sci. Adv. **9**, eadf2398 (2023). https://doi.org/10.1126/sciadv.adf2398
10. B. Chen, X. Zhong, G. Zhou, N. Zhao, H. Cheng, Graphene-supported atomically dispersed metals as bifunctional catalysts for next-generation batteries based on conversion reactions. Adv. Mater. **34**, 2105812 (2022). https://doi.org/10.1002/adma.202105812
11. Y. Sun, S. Dai, High-entropy materials for catalysis: a new frontier. Sci. Adv. **7**, eabg1600 (2021). https://doi.org/10.1126/sciadv.abg1600
12. Y. Xin, S. Li, Y. Qian, W. Zhu, H. Yuan et al., High-entropy alloys as a platform for catalysis: progress, challenges, and opportunities. ACS Catal. **10**, 11280–11306 (2020). https://doi.org/10.1021/acscatal.0c03617
13. P. Zhang, X. Hui, Y. Nie, R. Wang, C. Wang et al., New conceptual catalyst on spatial high-entropy alloy heterostructures for high-performance Li–$O_2$ batteries. Small **19**, 2206742 (2023). https://doi.org/10.1002/smll.202206742
14. X. Wang, Q. Dong, H. Qiao, Z. Huang, M.T. Saray et al., Continuous synthesis of hollow high-entropy nanoparticles for energy and catalysis applications. Adv. Mater. **32**, 2002853 (2020). https://doi.org/10.1002/adma.202002853
15. G.S. Hegde, R. Sundara, Entropy stabilized oxide nanocrystals as reaction promoters in lithium–$O_2$ batteries. Batter. Supercaps **5**, e202200068 (2022). https://doi.org/10.1002/batt.202200068
16. B. Hammer, J.K. Norskov, Why gold is the noblest of all the metals. Nature **376**, 238–240 (1995). https://doi.org/10.1038/376238a0
17. F. Li, M. Li, H. Wang, X. Wang, L. Zheng et al., Oxygen vacancy-mediated growth of amorphous discharge products toward an ultrawide band light-assisted Li–$O_2$ batteries. Adv. Mater. **34**, 2107826 (2022). https://doi.org/10.1002/adma.202107826
18. X. Li, G. Han, Z. Qian, Q. Liu, Z. Qiang et al., π-conjugation induced anchoring of ferrocene on graphdiyne enable shuttle-free redox mediation in lithium–oxygen batteries. Adv. Sci. **9**, 2103964 (2022). https://doi.org/10.1002/advs.202103964
19. X. Li, Z. Qian, G. Han, B. Sun, P. Zuo et al., Perovskite $LaCo_x Mn_{1-x} O_{3-\sigma}$ with tunable defect and surface structures as cathode catalysts for Li–$O_2$ batteries. ACS Appl. Mater. Interfaces **12**, 10452–10460 (2020). https://doi.org/10.1021/acsami.9b21904
20. Z. Li, Q. Wang, X. Bai, M. Wang, Z. Yang et al., Doping-modulated strain control of bifunctional electrocatalysis for rechargeable zinc–air batteries. Energy Environ. Sci. **14**, 5035–5043 (2021). https://doi.org/10.1039/D1EE01271A
21. W. Zhao, J. Wang, R. Yin, B. Li, X. Huang et al., Single-atom Pt supported on holey ultrathin g-$C_3N_4$ nanosheets as efficient catalyst for Li–$O_2$ batteries. J. Colloid Interface Sci. **564**, 28–36 (2020). https://doi.org/10.1016/j.jcis.2019.12.102
22. Y. Gong, W. Ding, Z. Li, R. Su, X. Zhang et al., Inverse spinel cobalt-iron oxide and N-Doped graphene composite as an efficient and durable bifuctional catalyst for Li–$O_2$ batteries. ACS Catal. **8**, 4082–4090 (2018). https://doi.org/10.1021/acscatal.7b04401
23. G. Zhang, G. Li, J. Wang, H. Tong, J. Wang et al., 2D SnSe cathode catalyst featuring an efficient facet-dependent selective $Li_2O_2$ growth/decomposition for Li–oxygen batteries. Adv. Energy Mater. **12**, 2103910 (2022). https://doi.org/10.1002/aenm.202103910
24. Z. Sun, X. Cao, M. Tian, K. Zeng, Y. Jiang et al., Synergized multimetal oxides with amorphous/crystalline heterostructure as efficient electrocatalysts for lithium–oxygen batteries. Adv. Energy Mater. **11**, 2100110 (2021). https://doi.org/10.1002/aenm.202100110
25. X. Han, L. Zhao, Y. Liang, J. Wang, Y. Long et al., Interfacial electron redistribution on lattice-matching $NiS_2$/$NiSe_2$ homologous heterocages with dual-phase synergy to tune the formation routes of $Li_2O_2$. Adv. Energy Mater. **12**, 2202747 (2022). https://doi.org/10.1002/aenm.202202747
26. G. Zhang, C. Liu, L. Guo, R. Liu, L. Miao et al., Electronic "bridge" construction via Ag intercalation to diminish catalytic anisotropy for 2D tin diselenide cathode catalyst in lithium–oxygen batteries. Adv. Energy Mater. **12**, 2200791 (2022). https://doi.org/10.1002/aenm.202200791
27. P. Wang, C. Li, S. Dong, X. Ge, P. Zhang et al., Hierarchical $NiCo_2S_4$@NiO core–shell heterostructures as catalytic cathode for long-life Li–$O_2$ batteries. Adv. Energy Mater. **9**, 1900788 (2019). https://doi.org/10.1002/aenm.201900788
28. A. Dutta, K. Ito, A. Nomura, Y. Kubo, Quantitative delineation of the low energy decomposition pathway for lithium peroxide in lithium-oxygen battery. Adv. Sci. **7**, 2001660 (2020). https://doi.org/10.1002/advs.202001660
29. S. Lau, L.A. Archer, Nucleation and growth of lithium peroxide in the Li–$O_2$ battery. Nano Lett. **15**, 5995–6002 (2015). https://doi.org/10.1021/acs.nanolett.5b02149
30. E. Dickinson, H. Ekström, E. Fontes, COMSOL Multiphysics®: finite element software for electrochemical analysis. A mini-review. Electrochem. Commun. **40**, 71–74 (2014). https://doi.org/10.1016/j.elecom.2013.12.020
31. Y. Qiao, S. Wu, J. Yi, Y. Sun, S. Guo et al., From $O_2^-$ to $HO_2^-$: reducing by-products and overpotential in Li–$O_2$ batteries

by water addition. Angew. Chem. Int. Ed. **129**, 5042–5046 (2017). https://doi.org/10.1002/ange.201611122

32. Z. Zhao, L. Guo, Z. Peng, Lithium–oxygen chemistry at well-designed model interface probed by in situ spectroscopy coupled with theoretical calculations. Adv. Funct. Mater. (2023). https://doi.org/10.1002/adfm.202302000
33. B. Chen, D. Wang, J. Tan, Y. Liu, M. Jiao, Designing electrophilic and nucleophilic dual centers in the $ReS_2$ plane toward efficient bifunctional catalysts for Li–$CO_2$ Batteries. J. Am. Chem. Soc. **144**, 3106–3116 (2022). https://doi.org/10.1021/jacs.1c12096
34. Y. Song, F. Kong, X. Sun, Q. Liu, X. Li et al., Highly reversible solid-state lithium–oxygen batteries by size-matching between Fe–Fe cluster and $Li_{2-x}O_2$. Adv. Energy Mater. **13**, 2203660 (2022). https://doi.org/10.1002/aenm.202203660
35. Q. Lv, Z. Zhu, Y. Ni, B. Wen, Z. Jiang et al., Atomic ruthenium-riveted metal–organic framework with tunable d-band modulates oxygen redox for Lithium–oxygen batteries. J. Am. Chem. Soc. **144**, 23239–23246 (2022). https://doi.org/10.1021/jacs.2c11676
36. Z. Zhu, Q. Lv, Y. Ni, S. Gao et al., Internal electric field and interfacial bonding engineered step-scheme junction for a visible-light-involved lithium–oxygen battery. Angew. Chem. Int. Ed. **61**, e202116699 (2022). https://doi.org/10.1002/ange.202116699

 https://doi.org/10.1007/s40820-023-01275-3